Noname manuscript No.
(will be inserted by the editor)

Biomechanical modeling of metal screw loadings on the human vertebra

Leonardo Molinari · Cristina Falcinelli* · Alessio Gizzi · Alberto Di Martino

Received: date / Accepted: date

Abstract During spinal fusion surgery screws, insertion at an angle relative to the spine's long axis can provide a more favorable stress distribution and reduce failure events such as screw breakage and loosening. Finite element (FE) analysis can be employed for the biomechanical assessment of lumbar surgical implants, thus (i) identifying the optimal insertion path, (ii) preventing stress concentrations, and (iii) ensuring a lower incidence of failure. In the present work, a patient-specific FE model of L4 vertebra, virtually implanted with two pedicle screws, was obtained from diagnostic images and numerically investigated. Linearly elastic, inhomogeneous, and isotropic material properties have been assigned to bone based on density distributions reconstructed from the medical images. The mechanical response of the screws-vertebra sys-

Leonardo Molinari
Department of Engineering
Campus Bio-Medico University of Rome
Via A. del Portillo 21, 00128 Rome, Italy
E-mail: leonardo.molinari@alcampus.it

*Corresponding Author: Cristina Falcinelli
Department of Engineering
Campus Bio-Medico University of Rome
Via A. del Portillo 21, 00128 Rome, Italy
E-mail: c.falcinelli@unicampus.it

Alessio Gizzi
Department of Engineering
Campus Bio-Medico University of Rome
Via A. del Portillo 21, 00128 Rome, Italy
E-mail: a.gizzi@unicampus.it

Albero Di Martino
Department of Biomedical and Neuromotor Science DIBINEM
University of Bologna, Bologna, Italy
1^{st} Orthopaedic and Traumatologic Clinic
IRCCS Istituto Ortopedico Rizzoli, Bologna, Italy
E-mail: dimartino.cbm@gmail.com

tem was analyzed then through a progressive damage procedure, considering a stress-based criterion. Different screws insertion angles were simulated, as well as physiological loading conditions. Results show that, in each loading case, screw orientation influences the fracture mechanism (i.e., brittle or ductile one) and the fracture pattern, as well as the fracture load. Besides, stresses in trabecular bone and pedicle screws are significantly affected by the configuration of the screw. The caudomedial trajectory indicates the most safety case, leading to significantly lower stress concentrations in both trabecular bone and screws. Our findings aim to furnish a useful indication to surgeons regarding the screws insertion angle, further reducing the risk of failure and improving the clinical outcome of the fixation procedure.

Keywords Fracture Mechanics · Patient-specific FE modeling · Vertebra mechanics · Fixation · Screw orientation · Stress analysis

1 Introduction

Spinal fusion is a surgical procedure in which two or more vertebrae are permanently joined into one solid bone [1]. This technique is widely adopted to treat or relieve symptoms of many diseases of the spine such as tumors, spinal stenosis, herniated discs, degenerative disc disease, scoliosis, fractured vertebrae, and spinal instability [2,3]. Screws and rods are inserted to connect the vertebrae (screw fixation). After a surgical treatment requiring screw fixation, localized bone failure events and screw loosening may occur due to stress shielding, bone micro-fractures, high strains and stresses at the bone-screws interface, causing the implant failure [6,4,5]. Also, the insertion trajectory of pedicle screws (i.e., the pedicle screws insertion angle) plays a major role in developing loosening phenomena [7]. As such, some clinical/experimental studies have been focused on investigating the effects of pedicle screws orientation through mechanical tests [3,8,9]. Sterba et al. [3], in cadaveric human vertebrae, compared pedicle screws with a straight to lateral angulation in the axial plane, demonstrating that laterally placed screws are more stable and less damaged after cyclic loading. The screw angle has been also investigated by Inceoglu et al. [8] using pedicle screw pullout tests. They found that a screw placed laterally angulated was characterized by a greater pullout strength compared to a straight insertion. On the contrary, Crawford et al. [9] found no significant differences in terms of pedicle screw pullout strength varying screw angle insertion in the axial plane.

Nowadays, the finite element (FE) method represents a powerful tool for the in-vitro and in-vivo characterization of the mechanical response of vertebrae [10]. FE models derived from computed-tomography (CT) biomedical images allow accounting for patient-specific vertebral geometry and heterogeneous bone density distribution [11]. Hence, FE tools permit to find the best fit for the implant as well as reduce possible failure scenarios.

Using FE modeling and analysis, Newcomb et al. [6] investigated different screw angles on a cohort of seven cadaveric L4 vertebrae, simulating multi-

directional loading and considering a single screw inserted in each vertebra. They showed that the insertion of screws at an angle relative to the long axis of the spine during fixation can represent a successful procedure to reduce the failure event, providing an advantageous stress distribution. Matsukawa et al. [12] also compared, by finite element analysis, the performance of the traditional and cortical bone trajectory (CBT), consisting of a divergent and caudocephalad screw path through the pedicle that engages only cortical bone. The author demonstrated that the CBT technique, even with shorter and smaller screws, provided higher pullout strength (26.4% greater mean pullout strength) and stronger stiffness (27.8% increase during cephalocaudal loading and 140.2% during mediolateral loading) compared to the traditional trajectory. The biomechanical effects of screw angulation on construct stability have been investigated by Hussain et al. [13] in cervical spine fixation by FE modeling and analysis. The authors showed that construct stability resulted independent of screw configurations, though higher stresses were detected at the bone-screw interface by increasing the screw angulations.

To the best of authors' knowledge, the effects of variation of screw insertion angle on fracture mechanics of instrumented vertebrae have not been investigated in terms of fracture load, fracture mechanism, and stress distribution. As such, the present work aims to evaluate, through an extended FE analysis, the mechanical response of L4 vertebrae after fixation, by varying the screw insertion angle. The final goal is to understand the impact of configuration angular parameters on fracture pattern/mechanisms and stress distribution in a patient-specific computational model.

The paper is organized as follows. Section 2 describes the image-based finite element strategy adopted in the present work and the associated boundary conditions. The numerical analyses are also presented, as well as the FE-based outputs. Section 3 furnishes the main results in terms of fracture patterns/mechanisms and stress distributions. The results are discussed in Section 4 highlighting model limitations and future perspectives.

2 Materials and Methods

2.1 Patient data

A computed tomography (CT) scan of the spine was performed on a female patient (49 years old) (SOMATOM Sensation 64 Siemens Healthineers AG, Munich, Germany; 120 kVp, 489 mA, 0.8418 $\times$ 0.8418 mm pixel size, 1 mm slice thickness) due to a recent trauma. The image analysis did not reveal previous spinal fractures. Before usage, the patient's data were anonymized.

2.2 Image-based FE screws-vertebra model

Geometry. First, from CT images, the geometry of the L4 vertebra has been reconstructed through a semi-automatic segmentation procedure (ITK-SNAP

3.8.0, University of Pennsylvania, Philadelphia, PA, USA) (Fig. 1, panels A and B). Then, CAD models of two non-cannulated pedicle screws were designed. The solid screws were cylindrical, with a length of 40 mm. The major and minor diameters of screws were 6.5 mm and 4.3 mm, respectively. The thread depth was 1.1 mm and each thread pitch was 3 mm. The CAD model of the non-cannulated pedicle screws was presented with dimensions in Figure 1 (panel C).

Screws virtual implantation. Nine different screws insertion paths were investigated. All the analyzed trajectories were considered as starting from the same insertion points, established following clinical indications for a transpedicular convergent trajectory, widely adopted during surgical procedures. In detail, both screws have been virtually inserted to a depth of 30 mm and then simultaneously rotated around their insertion points in two directions, i.e. mediolateral and craniocaudal directions. The procedure adopted in the present study does not mimic the procedure used in a real surgery of screw fixation. In a real surgery, the surgeon identifies the screw insertion point, and opens the superficial cortex of the entry point and inserts a probe to navigate down the isthmus of the pedicle into the vertebral body with an appropriate trajectory in craniocaudal and mediolateral directions. Finally, the probe is removed and the pedicle screws are carefully inserted into the same created trajectory. In the present study, we simulated the insertion and the rotation of screws to maintain fixed the entry point, and guarantee different trajectories with the rotations. As a result, the nine trajectories were obtained by combining three craniocaudal (-5, 0, 5)° and three mediolateral (-5, 0, 5)° insertion angles. The neutral trajectory has been assumed characterized by 0° in the craniocaudal direction and 0° in the mediolateral direction. With respect to the neutral configuration, a positive rotation in the craniocaudal plane means a cranial insertion whereas a negative rotation means a caudal insertion. Similarly, a positive rotation in mediolateral direction means a lateral insertion whereas a negative one means a medial insertion. As a notation rule, the vector $\vec{\boldsymbol{\alpha}}$ identifies a specific screws combination as reported in the following expression:

$$\vec{\boldsymbol{\alpha}} = [\alpha_1, \alpha_2] \tag{1}$$

where α_1 indicates the insertion angle in craniocaudal direction and α_2 the insertion angle in mediolateral direction. As an example, the expression $\vec{\boldsymbol{\alpha}} = [5, -5]$ indicates that screws are inserted with a positive angle of 5° in the craniocaudal direction and a negative angle of 5° in the mediolateral direction.

Once the entry points and the insertion directions have been identified, a boolean operation was performed in the vertebra model to remove bone at the location of the screws and thus simulate the screws implant. The resulted screws-vertebra solid model and the convention used to define the craniocaudal and mediolateral orientations are reported in Figure 1 (panels D and E).

Computational discretization. Complete three-dimensional solid model was imported within the Comsol environment (Comsol, 5.5, COMSOL, Stockholm,

Sweden) to create the computational discretization. In detail, the screws-vertebra assembly has been discretized by using second-order displacement-based tetrahedral elements, resulting in an unstructured topology (Fig. 1, panel F). A preliminary convergence analysis has been carried out to establish the mesh size and refinement for the vertebra (Section 3.1). Then, the element dimension for the screws mesh has been set as half the size of the vertebra ones.

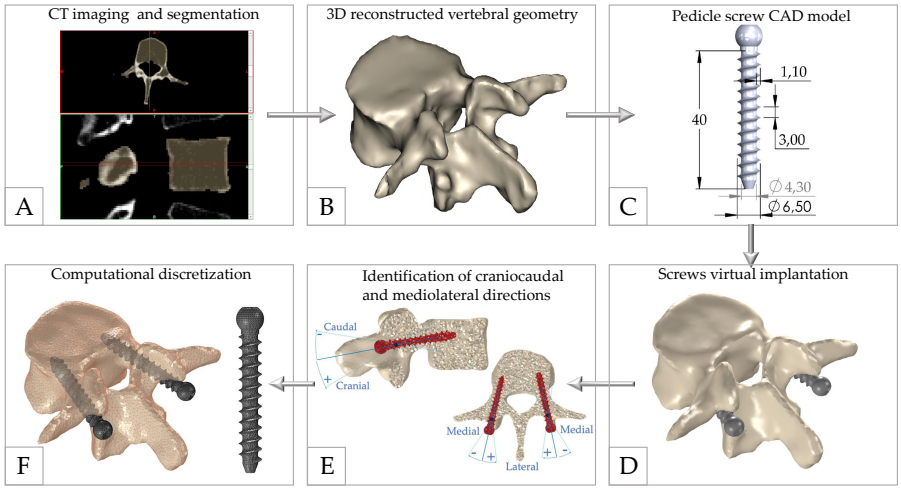

Fig. 1 Image-based FE modeling procedure. Starting from CT images (A), the vertebral geometry is reconstructed through segmentation (B). Then, the CAD models are designed for two pedicle screws, whose characteristics are reported in panel C. The pedicle screws are virtually inserted with a depth of 30 mm (D) and then simultaneously rotated around their insertion points in mediolateral and craniocaudal directions (E). Finally, the computational vertebra-screws domain is discretized through an unstructured mesh (F).

Constitutive modeling and material identification. Isotropic and linearly elastic material properties with an heterogeneous Young's Modulus E [14] and a constant Poisson's ratio ν (ν=0.3) [15] have been considered for the vertebra. The heterogeneous distribution of material stiffness has been derived from CT data adopting a two-steps procedure implemented in Matlab. The first step was characterized by the application of a customized artifacts-removal algorithm to ensure that the physiological boundaries of the cortical layer are accurately detected. This is a crucial step due to the fact that the cortex layer in the vertebra is very thin and the resolution of a clinical CT scan is not able to well-identify such a small structure. As such, partial volume artifacts (PVEs) are usually present, leading to underestimation of HU and thus of bone density and Young's modulus E [16]. The application of a such algorithm allows to reduce the PVEs and avoids that the adjacent soft tissues influence the CT data

interpolation and thus the elasticity values. The artifacts-removal algorithm first identifies the CT voxels outside of the vertebral region. Then, it separates the voxels that belong to the segmented bone domain in two surbegions (i.e., cortical and trabecular subregions labelled as Ω_C and Ω_T, respectively) based on a HU threshold value equal to 700. In detail, Ω_C was identified by the voxels with HU$\geq$700, whereas Ω_T by the voxels with HU$<$700. At this point, the algorithm averages the HU values of voxels of Ω_C to extract a representative HU value and assign it to voxels outside the vertebra domain. In the present work a value of 923 has been obtained as representative HU value. Finally, a moving average filter with a box size of $5 \times 5 \times 5$ voxels was implemented to smooth out the HU spatial distribution and thus avoid low values of HU and thus of Young's modulus on the outer surface of the vertebra. Figure 2 shows Young's modulus distribution of vertebra before and after filtering highlighting the capability of the adopted strategy to detect the thin cortical layer.

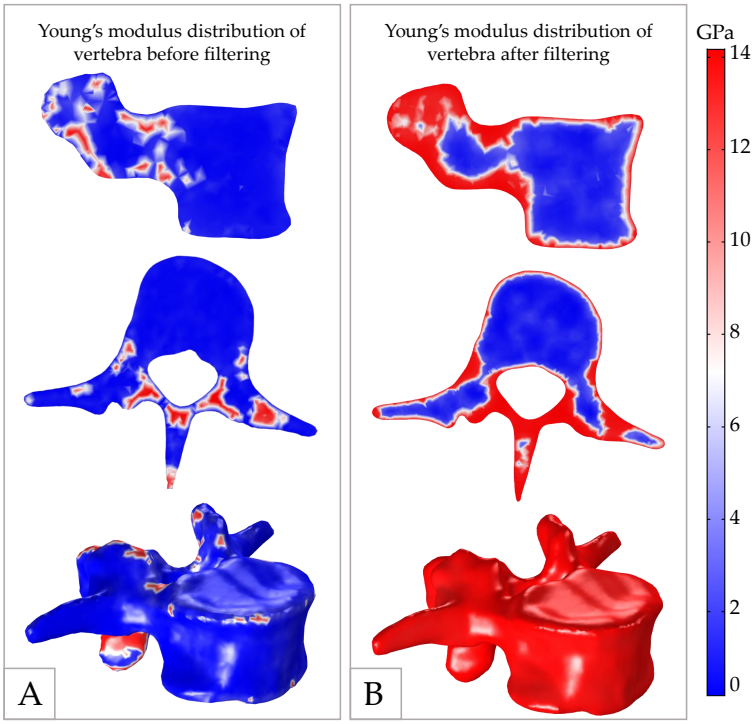

Fig. 2 Young's modulus (GPa) distribution of vertebra before (A) and after (B) filtering. As shown in panel B, filtering allows to detect the thin cortical layer that characterizes vertebrae.

The second step of the procedure to derive the heterogeneous distribution of material stiffness from CT data is characterized by the transformation of the heterogeneous HU distribution into an heterogeneous distribution of E. The HU values obtained from the artifacts-removal algorithm were interpolated over the mesh nodes and converted in apparent density ρ_{app} through the following ρ_{app} - HU relationship, where ρ_{app} is expressed in g/cm^3:

$$\rho_{app} = 1.9 \times HU/1109 \tag{2}$$

Due to the absence of a calibration phantom, the Equation 2 has been determined through a linear correlation between HU and ρ_{app} by considering that HU=0 corresponded to a ρ_{app}=0 and the maximum filtered value of HU = 1109 corresponded to a ρ_{app}=1.9 g/cm^3 [17]. An apparent density of 1.9 g/cm^3 represents the maximum value of the apparent density for cortical bone [18]. Negative values of ρ_{app} were set to zero to avoid unrealistic density values and numerical issues. The resulted heterogeneous ρ_{app} distribution was converted to ash density (ρ_{ash}) expressed in g/cm^3 using the relationship adopted by Keyak et al. [19]:

$$\rho_{ash} = 0.551 \times \rho_{app} - 0.00478 \tag{3}$$

Then, the following relations were used to determine the Young's Modulus for trabecular (E_T) and cortical (E_C) bone, expressed in MPa, starting from ρ_{app}:

$$E_T = 4730 \times \rho_{app}^{1.56} \tag{4}$$

$$E_C = -892.5 \times \rho_{app}^{-2.491} + 14360 \tag{5}$$

The relation adopted for trabecular bone (Eq. 4) has been proposed by Morgan et al. [20], whereas for cortical bone a custom-made equation (Eq. 5) has been adopted whose details have been reported in Appendix A. Equations 4 and 5 allow to obtain an elastic modulus ranging between 0 and 3 GPa for trabecular bone and between 12 and 14 GPa for cortical bone. Finally, compressive (σ^-) and tensile (σ^+) yield stresses (MPa) have been obtained by the following equations according with [19,21]:

$$\sigma_T^- = 137 \times \rho_{ash}^{1.88} \tag{6}$$

$$\sigma_C^- = 114 \times \rho_{ash}^{1.72} \tag{7}$$

$$\sigma^+ = 0.8 \times \sigma^- \tag{8}$$

For the pedicle screws, an elastic modulus of 110 GPa and a Poisson's ratio of 0.4 were chosen, corresponding to the mechanical properties of Ti-6Al-4V (UNS R56400). Similarly to the bone, the screws mechanical behavior was considered isotropic and linear elastic.

2.3 Boundary conditions

In the present study, boundary conditions are chosen to mimic physiological motions. In detail, six different loading modes have been considered corresponding to the following body positions:

- flexion (FLEX) and extension (EXT);
- counter-clockwise axial rotation (CCR) and clockwise axial rotation (CR);
- left and right lateral bending (LLB and RLB, respectively).

Figure 3 (panel A) shows the regions were forces and boundary conditions have been applied: 1) inferior endplate, 2) superior endplate and 3) articular facets. The inferior endplate of the L4 vertebra in all tested loading conditions was fully constrained in all degrees of freedom (Fig. 3 panel B). Conversely to the most of the works reported in the literature, in which the load is applied only to the implant and the vertebra is fixed or vice versa [12,22,6], in the present work screws and vertebra have been loaded simultaneously. In detail, the total compressive load has been distributed among the vertebral body ($F_{vertebra}$, applied on the top endplate), the articular facets ($F_{articular}$ applied on the articular facets) and the screw heads, as shown in Figure 3 (panel B). The amount of the load applied on the screws (20% of the total load) has been applied in different directions based on the specific loading mode (Fig. 3 (panel B)). In addition, a uniform moment (4.7 Nm) [23] has been applied along the three directions reported in Figure 3 (panel B). The center of the L5-S1 intervertebral disc has been assumed as the rotation center. For each loading mode, pedicle screws and vertebral bone have been assumed bonded, according to previous works reported in the literature [22,24].

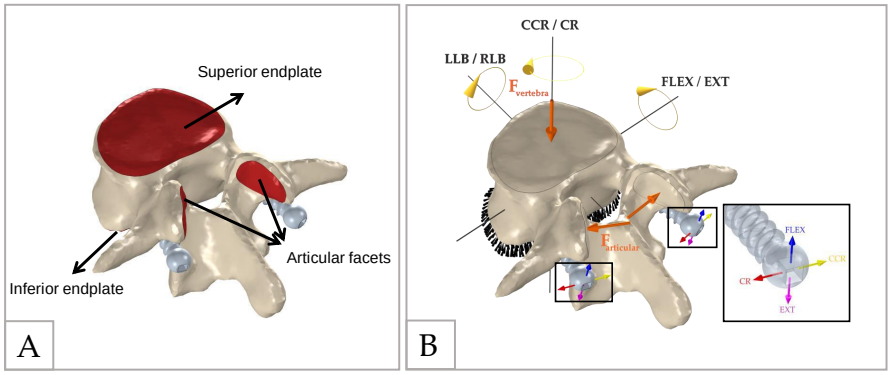

Fig. 3 Boundary conditions employed for numerical analyses. A) In red the regions where forces and boundary conditions have been applied are shown. B) Compressive force ($F_{vertebra}$) and articular force ($F_{articular}$) have been applied to the superior endplate of the vertebral body and the articular facets, respectively. Moreover, the screw heads have been loaded with a force applied in different directions based on the specific loading mode. The inferior endplate has been fully constrained.

2.4 Failure criterion

A maximum principal stress criterion has been adopted. In this case, bone is considered locally failed in compression or tension if

$$\sigma^{-}_{EQ} > \sigma^{-} \tag{9}$$

$$\sigma^{+}_{EQ} > \sigma^{+} \tag{10}$$

where σ^{-} and σ^{+} are the density-based yield stresses obtained from the Equations 6, 7 and 8. The terms σ^{-}_{EQ} and σ^{+}_{EQ} represent local stress measures defined in terms of principal stresses σ_1, σ_2 and σ_3 as:

$$\sigma^{-}_{EQ} = -\min\{0, \sigma_1, \sigma_2, \sigma_3\} \tag{11}$$

$$\sigma^{+}_{EQ} = \max\{0, \sigma_1, \sigma_2, \sigma_3\} \tag{12}$$

Degradation rule. When the failure criterion is locally verified, local constitutive degradation of the vertebral bone is assumed. In detail, the degradation rule implies that the Young's Modulus of the failed elements is set to 10^{-6} MPa leading to an update of model material properties. The failed elements identify the fracture pattern.

2.5 Numerical analyses

A numerical iterative procedure was implemented by developing a custom Matlab code that has been integrated within the commercial FE solver Comsol Multiphysics (Fig. 4).

The local progressive vertebral damage has been simulated by a quasi-static force-driven incremental approach. Assuming that F^i is the total force at the i-th step, the total force at the step $i+1$ (labeled as F^{i+1}) is obtained as

$$F^{i+1} = F^i + \lambda \Delta F \tag{13}$$

where ΔF is the constant load increment assumed equal to 100 N and λ is a load rate assumed as inversely proportional to the ratio of the fractured to the total elements. At each incremental step, the solution in terms of stress and strain fields, as well as in terms of vertebral reaction force (F^V), are calculated and the failure occurrence is verified by using the failure criterion reported in Section 2.4. If bone failure is not detected, the applied force is increased based on the Equation 13 and a new incremental step is computed. Conversely, the FE model is updated by following the degradation rule reported in Section 2.4, and the actual step is iteratively repeated until further bone failure is no longer detected. The complete failure of the vertebra occurs when such a procedure does not converge.

At each incremental step F^V is calculated by computing a numerical integration of the incremental reaction forces on the L4 superior endplate. Finally, the maximum load value recorded before an abrupt increase in the superior

endplate displacement occurs is considered the ultimate force F_{ult}^{V}, i.e. the fracture load.

Fifty-four numerical analyses have been performed (six loading modes differentiated among 9 screw configuration angles). The overall computational time was bout 8 days on an HP Z640 workstation with E5-2630 v3 (8 $\times$ 2.40 GHz) and 32 GB of RAM.

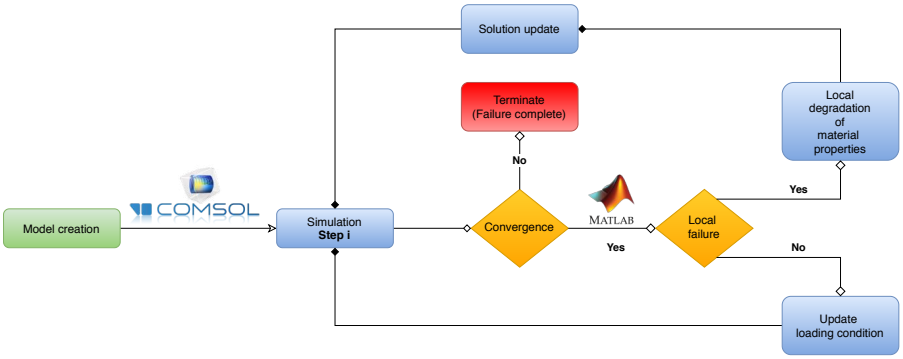

Fig. 4 Flow diagram of the numerical procedure adopted to investigate the mechanical behavior of vertebra.

2.6 Post-processing

For each loading mode and insertion angle, the force-displacement curve has been analyzed, the F_{ult}^{V} (Sec. 2.5), and the fracture mechanism defined. In detail, the fracture has been considered ductile-like if the force-displacement curve was characterized by a larger ultimate displacement, resulting in increased work to failure. On the contrary, the fracture has been classified as brittle if the force-displacement curve showed a smaller ultimate displacement (resulting in a reduced work to failure).

For each loading condition and insertion angle, Von mises and maximum stresses (σ_{VM} and $\sigma_{\max}$, respectively) have been separately computed on cortical bone, trabecular bone, and screws.

2.7 Statistical analysis

In terms of statistical analysis, a one-way ANOVA test has been adopted to investigate the influence of screw insertion angles. The statistical assumptions of ANOVA were first verified. In detail, the Shapiro-Wilk test was used to verify the normality of data, whereas the Levene's test was adopted to confirm the homogeneity of the variance across groups. If these assumptions were not satisfied, a non-parametric alternative to a one-way ANOVA test, i.e. the

Kruskal-Wallis test, has been adopted. When the ANOVA test or Kruskal-Wallis test revealed significant differences, pairwise multiple comparisons test (i.e., the Tukey-Kramer test) was performed to determine which pairs were significantly different. For all statistical tests, significance was set at p=0.05. All analyses were performed with the free statistical software R (https://CRAN.R-project.org).

3 Results

3.1 Convergence analysis

To provide accurate numerical results the mesh element size has been established based on a preliminary convergence analysis, performed on the uninstrumented L4 vertebra model. Eleven different mesh refinements (Table 1) have been considered characterized by a maximum element size d_{max} varying in the range from 1.5 mm to 6 mm. Moreover, the minimum mesh element size d_{min} has been set as $d_{min} = d_{max}/2$ to obtain a uniform mesh.

Table 1 Mesh refinements (MR) used for convergence analysis. Numerical solution obtained with MR11 as reference solution. # Number of elements; $d_{\max}, d_{\min}, \bar{d}$ in [mm].

	MR1	MR2	MR3	MR4	MR5	MR6	MR7	MR8	MR9	MR10	MR11
$d_{\max}$	6	4	3.5	3	2.5	2.2	2	1.90	1.8	1.7	1.6
$d_{\min}$	3	2	1.75	1.5	1.25	1.1	1	0.95	0.9	0.85	0.8
$\bar{d}$	5.06	3.45	3.04	2.61	2.17	1.91	1.73	1.65	1.56	1.47	1.40
#	11120	27739	39884	62688	107240	158728	212089	248728	291875	346857	416157

For each mesh refinement the relative strain energy difference (E_{W_s}) and the relative Von Mises stress difference ($E_{\sigma_{\mathrm{VM}}}$) with respect to the reference solution have been computed, assuming the finest discretization (i.e., MR11 in Table 1) as the reference solution. In addition, for each computational discretization fracture type (i.e., ductile-like or brittle-like fracture, see Section 3.2.1) and fracture pattern have been analyzed.

In terms of fracture type, all mesh refinements have exhibited a ductile-like fracture, except for MR1 that has showed a brittle-like one. In Figure 5 the fracture pattern obtained for each mesh refinement has been reported showing no significant differences among the different meshes. Figure 6 shows the relative strain energy difference estimates versus the mean mesh element size ($\bar{d}$). Accordingly, convergence could be considered achieved for the MR4 model with $E_{W_s} \simeq 5\%$. A relative difference of 5% or less can be considered acceptable according to [10]. However, the relative difference in terms of Von Mises stress was greater than 10% for model MR4. To obtain the convergence in terms of both parameters, the model characterized by both the E_{W_s} and $E_{\sigma_{\mathrm{VM}}}$ equal or lower than 5% has been chosen. As such, MR7 was selected because it showed a relative strain energy difference of 2% and a relative Von

Mises stress difference equal to 4% (Table 2). Computational models employed to perform numerical simulations have been defined by considering d_{max} and d_{min} equal to 2 and 1 mm, respectively, obtaining a good compromise between computational costs and numerical accuracy.

According to Section 2.2, screws were meshed with minimum and maximum elements size of 0.1 mm and 1 mm, respectively, resulting in 6.2×10^4 elements. The whole instrumented vertebra FE model is then characterized by 2.7×10^5 elements and 1×10^6 degrees of freedom.

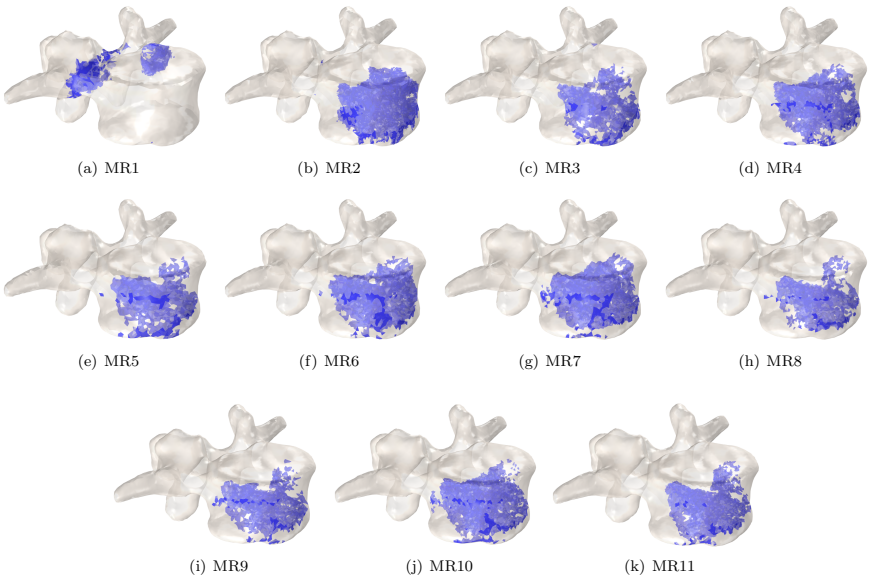

(a) MR1 (b) MR2 (c) MR3 (d) MR4

(e) MR5 (f) MR6 (g) MR7 (h) MR8

(i) MR9 (j) MR10 (k) MR11

Fig. 5 Fracture patterns for all mesh refinements obtained in the convergence analysis. All meshes show a similar fracture pattern, except for MR1. This difference could be related to the too coarse mesh adopted for MR1 that also has led to high errors in terms of E_{W_s} and $E_{\sigma_{\mathrm{VM}}}$ (see Table 2).

Table 2 Relative strain energy and Von Mises stress differences (E_{W_s} and $E_{\sigma_{\mathrm{VM}}}$, respectively) computed for each mesh refinement (MR) with respect to the MR11 (Table 1) assumed as the reference solution.

	Δ_{MR1}	Δ_{MR2}	Δ_{MR3}	Δ_{MR4}	Δ_{MR5}	Δ_{MR6}	Δ_{MR7}	Δ_{MR8}	Δ_{MR9}	Δ_{MR10}
E_{W_s}	26%	10%	10%	5%	1%	2%	2%	2%	0%	1%
$E_{\sigma_{\mathrm{VM}}}$	42%	22%	17%	11%	7%	5%	4%	3%	2%	1%

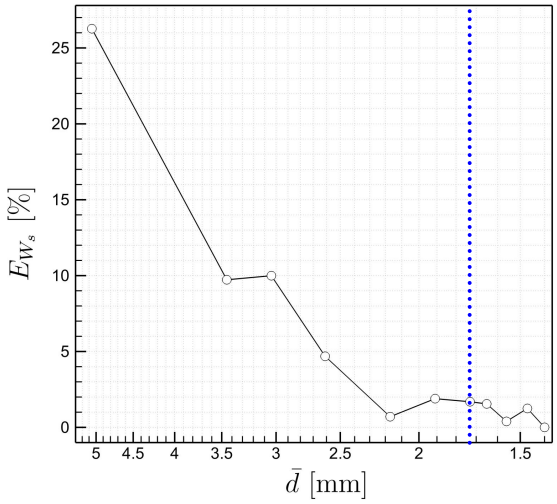

Fig. 6 Relative strain energy difference (E_{W_s}) versus the average mesh dimension $\bar{d}$ computed analyzing the uninstrumented L4 model under flexion. Convergence is achieved for MR7 model (identified by the vertical dashed line) with $E_{W_s} \simeq 2\%$ with respect to the reference solution (MR11).

3.2 Comparative analysis

3.2.1 Fracture patterns and mechanisms

The analysis of force-displacement curves obtained from FE analyses revealed that the 83% of fractures highlighted a brittle behavior, whereas the remaining 17% exhibited a ductile-like response. Figure 7 shows an example of the force-displacement curve obtained for brittle-like and ductile-like fractures. The brittle curve has been obtained for $\vec{\boldsymbol{\alpha}} = [5, 5]$ in CR loading condition, whereas the ductile one for $\vec{\boldsymbol{\alpha}} = [-5, -5]$ in EXT loading mode. Looking at Fig. 7, the curve that describes the brittle behavior shows a severe increase of fracture load at a constant displacement before fracture. This behavior could be associated with a local stress intensification that could be related to the presence and propagation of crack fracture.

Table 3 summarizes the fracture loads (expressed in N) and mechanism (brittle or ductile) detected by numerical simulations for all analyzed loading modes and insertion angles. Fracture loads ranged from 3139 N (FLEX, $\vec{\boldsymbol{\alpha}} = [-5, 0]$) to 7680 N (CR, $\vec{\boldsymbol{\alpha}} = [5, 0]$).

Looking at the ductile-like behavior, fracture patterns originated in the posterior zone and moved anteriorly involving a large portion of the vertebral body that is characterized by a large amount of trabecular bone (Fig. 8(a)). Conversely, the brittle fracture involved mainly the pedicular region that is characterized by cortical bone. In addition, for brittle-like behavior symmetrical and asymmetrical patterns have been observed (Figs. 8(b) and 8(c)). Flexion and extension loading modes showed symmetrical patterns for

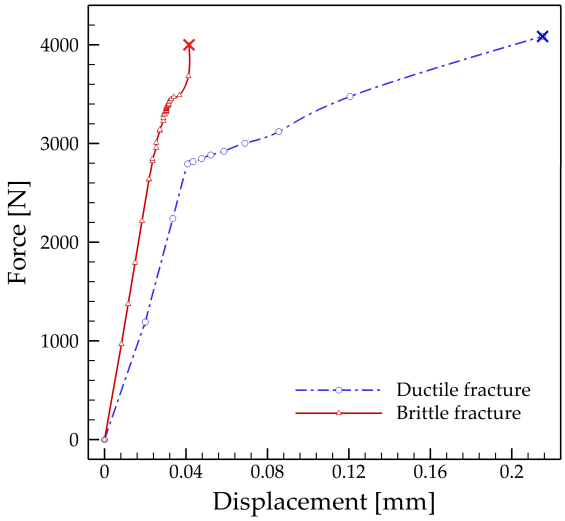

Fig. 7 Force-displacement curves for the brittle-like (red solid line) and ductile-like (blu dashed line) fractures. The brittle curve has been obtained for $\vec{\boldsymbol{\alpha}} = [5, 5]$ in CR loading condition, whereas the ductile one for $\vec{\boldsymbol{\alpha}} = [-5, -5]$ in EXT loading mode. For sake of readability, only two cases have been reported.

all screws insertion angles with exception of flexion loading mode characterized by $\vec{\boldsymbol{\alpha}} = [-5, 5]$ for which an asymmetrical pattern has been observed. Asymmetric paths were associated with CR, CCR, LLB, and RLB loading conditions with some exceptions reported in Table 4 for which symmetrical patterns have been obtained.

Table 3 Fracture loads, F^V_{ult} (N), and fracture mechanisms, FM, for screws-vertebra models computed combining different loading conditions and screws insertion angle $\vec{\boldsymbol{\alpha}} = [\alpha_1, \alpha_2]$). Brittle or ductile fracture mechanism are indicated with B or D, respectively.

$\vec{\boldsymbol{\alpha}}$	Loading conditions											
	FLEX		EXT		CCR		CR		LLB		RLB	
	F^V_{ult} (N)	FM	F^V_{ult} (N)	FM	F^V_{ult} (N)	FM	F^V_{ult} (N)	FM	F^V_{ult} (N)	FM	F^V_{ult} (N)	FM
$[0, 0]$	3278	B	4431	B	3699	B	4547	B	3531	B	3551	B
$[0, 5]$	3626	B	4134	B	5563	B	4482	B	4369	B	3738	B
$[5, 5]$	4774	B	4793	B	5184	B	7261	B	3555	B	3683	B
$[5, 0]$	3668	B	4346	B	4120	B	7680	D	3641	B	3663	B
$[5, -5]$	3518	B	5603	B	4538	B	3877	B	3397	B	3499	B
$[0, -5]$	3372	B	6076	D	3850	B	6948	B	3579	B	3561	B
$[-5, -5]$	3194	D	4086	D	3255	D	4648	D	3550	D	5253	D
$[-5, 0]$	3139	B	5113	D	7488	B	3943	B	3612	B	3628	B
$[-5, 5]$	3577	B	3393	B	4695	B	4247	B	3289	B	3281	B

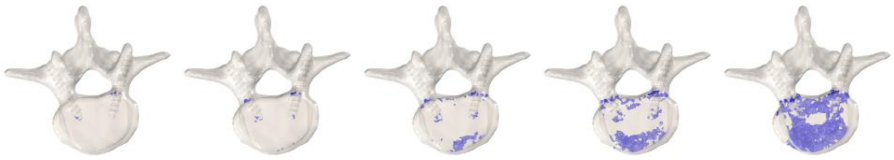

(a) Ductile fracture pattern

(b) Brittle fracture characterized by a symmetrical path

(c) Brittle fracture characterized by an asymmetrical path

Fig. 8 Fracture patterns obtained by FE analysis: a) ductile-like fracture, b) brittle-like symmetrical fracture pattern and c) brittle-like asymmetrical fracture path.

Table 4 Screws insertions angles and corresponding loading condition for which symmetrical fracture paths have been obtained instead of expected asymmetric ones.

$\vec{\boldsymbol{\alpha}} = [\alpha_1, \alpha_2]$	Loading condition
$\vec{\boldsymbol{\alpha}} = [0, 5]$	LLB
$\vec{\boldsymbol{\alpha}} = [-5, 5]$	LLB
$\vec{\boldsymbol{\alpha}} = [-5, 5]$	RLB
$\vec{\boldsymbol{\alpha}} = [-5, -5]$	RLB
$\vec{\boldsymbol{\alpha}} = [-5, 5]$	CCR
$\vec{\boldsymbol{\alpha}} = [5, 0]$	CR
$\vec{\boldsymbol{\alpha}} = [-5, -5]$	CR

3.2.2 Stress analysis

In cortical bone, $\sigma_{\max}$ did not show significant differences among the different insertion angles (p-value equal to 0.11 - Kruskall-Wallis test). Instead, σ_{VM} was at the limit of significance (p-value=0.051 - Kruskall-Wallis test). The Tukey-Kramer test revealed significant differences in terms of σ_{VM} among $\vec{\boldsymbol{\alpha}} = [-5, -5]$ and $\vec{\boldsymbol{\alpha}} = [5, 5]$. Figure 9 shows the σ_{VM} distribution in cortical bone obtained from $\vec{\boldsymbol{\alpha}} = [-5, -5]$ and $\vec{\boldsymbol{\alpha}} = [5, 5]$ for each loading condition.

Significant differences have been obtained in trabecular bone in terms of $\sigma_{\max}$ and σ_{VM} (p-value=0.003 for $\sigma_{\max}$ and p-value<0.0001 for σ_{VM} - one-way ANOVA test). Figure 10 shows results obtained from Tukey-Kramer test. In

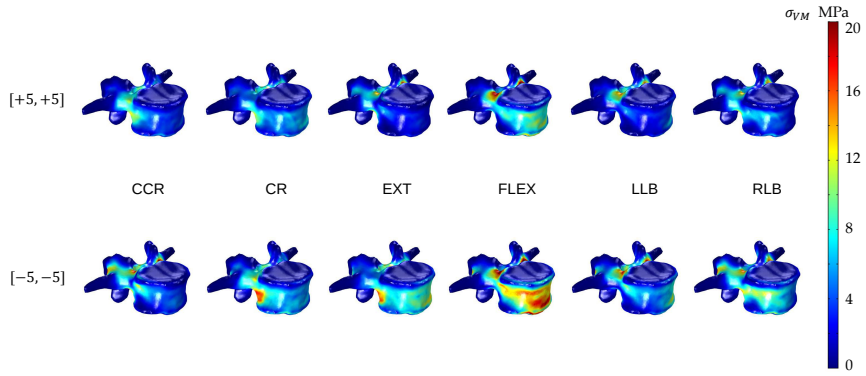

Fig. 9 The σ_{VM} distribution in cortical bone obtained from $\vec{\boldsymbol{\alpha}} = [5, 5]$ (top) and $\vec{\boldsymbol{\alpha}} = [-5, -5]$ (bottom) configurations for each loading condition.

detail, for $\sigma_{\max}$ seven groups resulted significant different from $\vec{\boldsymbol{\alpha}} = [-5, -5]$ (p-value<0.05) with the exception of $\vec{\boldsymbol{\alpha}} = [-5, 5]$ (Fig. 10(a)). For σ_{VM}, all groups resulted significant different from $\vec{\boldsymbol{\alpha}} = [-5, -5]$ (p-value<0.05, Fig. 10(b)). From Figs. 10 it can be also noticed that the insertion angle $\vec{\boldsymbol{\alpha}} = [-5, -5]$ exhibited lower stresses ($\sigma_{\max}$ and σ_{VM}) than other angles. This can be also observed in Fig. 11 where the $\sigma_{\max}$ contour plot has been reported for two cases, i.e. $\vec{\boldsymbol{\alpha}} = [-5, -5]$ and $\vec{\boldsymbol{\alpha}} = [0, -5]$. Figure 11 highlights that $\vec{\boldsymbol{\alpha}} = [-5, -5]$ develops lower stress concentrations than the $\vec{\boldsymbol{\alpha}} = [0, -5]$ configuration in trabecular bone.

Looking at the screws, significant differences have been obtained in terms of both $\sigma_{\max}$ (p-value=0.0068, Kruskal-Wallis test) and σ_{VM} (p-value=0.036, Kruskal-Wallis test). In addition, $\vec{\boldsymbol{\alpha}} = [-5, -5]$ resulted significantly different from $\vec{\boldsymbol{\alpha}} = [5, 5]$ and $\vec{\boldsymbol{\alpha}} = [5, 0]$ in terms of $\sigma_{\max}$ (p-value<0.05), whereas no significant differences among the pairs have been obtained in terms of σ_{VM}. Figure 12 shows the $\sigma_{\max}$ distributions for $\vec{\boldsymbol{\alpha}} = [-5, -5]$ and $\vec{\boldsymbol{\alpha}} = [5, 5]$, highlighting that $\vec{\boldsymbol{\alpha}} = [-5, -5]$ is characterized by lower stress concentrations compared to $\vec{\boldsymbol{\alpha}} = [5, 5]$.

In Appendix B, the results of Shapiro-Wilk and Levene's tests have been reported for each tested variable.

4 Discussion

Numerical results indicate that the screws insertion angle significantly affects the mechanical response of the vertebra in terms of fracture load, fracture mechanism, and stress distribution. Moreover, statistical analyses designate that among the several screws insertion trajectories, the caudomedial one, i.e. $\vec{\boldsymbol{\alpha}} = [-5, -5]$, results to be the safest in preventing vertebral fractures, and thus it should be preferred by surgeons to perform spinal fusion of lumbar

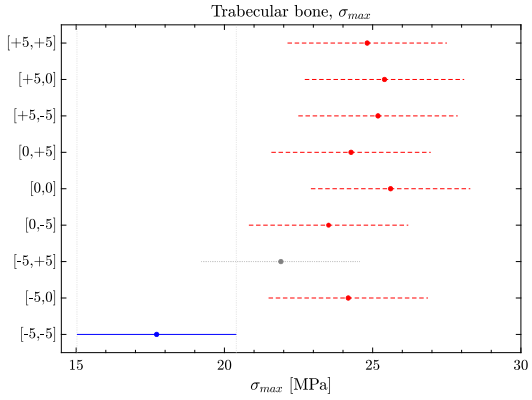

(a)

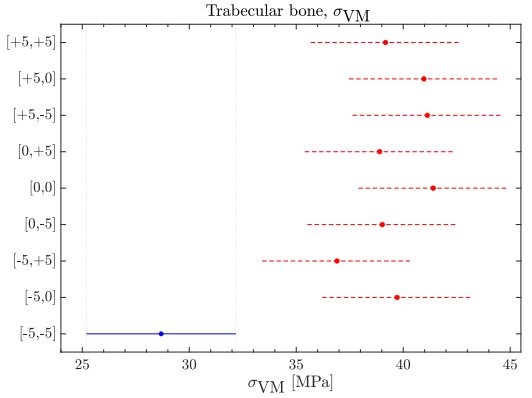

(b)

Fig. 10 Graphical representation of comparisons between screw insertion angles to identify the significant differences. On the top, the variable $\sigma_{\max}$ was tested, whereas in the bottom the variable σ_{VM} was considered. A solid line is significantly different from a dashed line, whereas a solid line and a dotted line or two dashed lines or a dashed line and a dotted one do not show a significant difference. As such, $\vec{\boldsymbol{\alpha}} = [-5, -5]$ is significantly different from all other configurations in terms of $\sigma_{\max}$, with the exception of $\vec{\boldsymbol{\alpha}} = [-5, 5]$. In terms of σ_{VM}, $\vec{\boldsymbol{\alpha}} = [-5, -5]$ shows significant differences with respect to all other configurations.

vertebrae. These results have been achieved by performing an extensive FE study on a bilaterally instrumented L4 vertebra to understand the impact of pedicle screw angles on fracture occurrence under physiological loading. Patient-specific vertebral geometry and material properties distribution have been derived from CT images. Nine pedicle screws trajectories have been tested in multiaxial loading.

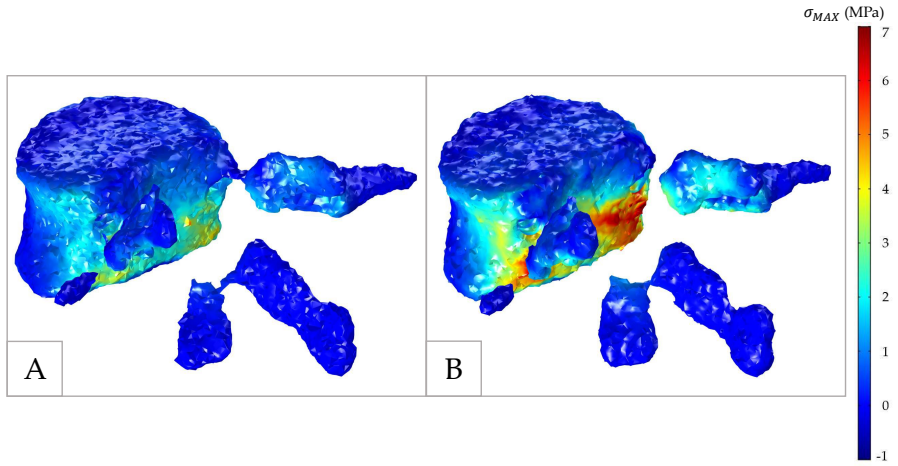

Fig. 11 The $\sigma_{\max}$ contour plots in trabecular bone obtained from $\vec{\boldsymbol{\alpha}} = [-5, -5]$ (panel A) and $\vec{\boldsymbol{\alpha}} = [0, -5]$ (panel B).

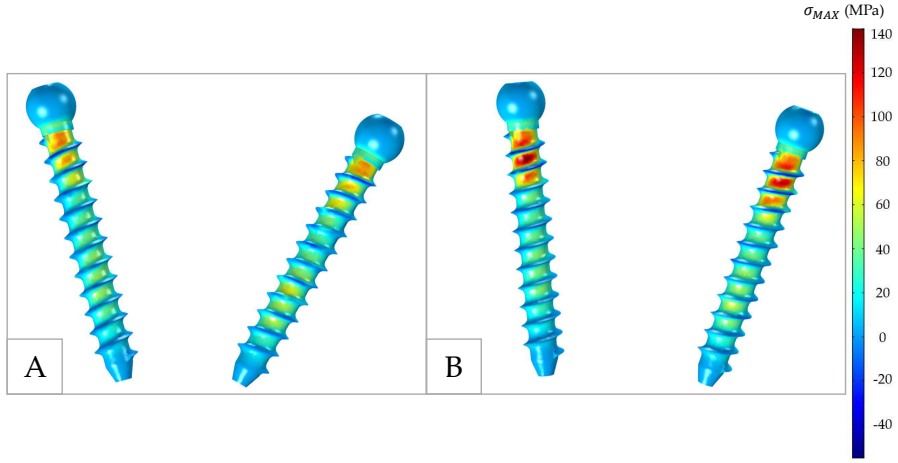

Fig. 12 The $\sigma_{\max}$ contour plots in pedicle screws obtained from $\vec{\boldsymbol{\alpha}} = [-5, -5]$ (panel A) and $\vec{\boldsymbol{\alpha}} = [5, 5]$ (panel B).

The influence of screws trajectories on the mechanical response of vertebra has been highlighted by the high variability in fracture load and fracture patterns that have been obtained in the different loading conditions. In most of the cases, the fracture exhibited a brittle behavior. Conversely, the configuration $\vec{\boldsymbol{\alpha}} = [-5, -5]$ exhibited a ductile mechanism for all tested loading. A ductile mechanism is surely more appropriate to describe the failure mechanism of vertebrae. Such a result can be explained by the large part of trabecular tissue

that characterizes the vertebral body. Trabecular bone can undergo large plastic deformations prior to the fracture in contrast to long bones that exhibit a brittle failure due to a large amount of cortical bone. A generalized analysis of bone plasticity calls for advanced constitutive and computational modeling approaches [25,26] we foresee to adopt in future studies.

The stress analysis performed independently for cortical bone, trabecular bone, and screws showed that the trajectory $\vec{\boldsymbol{\alpha}} = [-5, -5]$ may indicate better clinical outcomes in preventing excessive stresses in trabecular bone and screws. Reducing stresses in both trabecular bone and screws is important to avoid trabecular bone failure and subsequent screws loosening, as well as screws breakage. This finding is in agreement with the results found by Newcomb et al. [6].

Some limitations of the present work can be mentioned. First, the developed computational approach has been applied to only one vertebra without a prior experimental validation. Performing a validation through experimental measurements is crucial to translate computational approaches in the clinical practice [27]. However, the present study aimed to work with the current technology available in the hospitals and thus the present study can be considered a starting point for a feasible clinical application that won't have access to experimental measurements. As such, extending the study to a larger age-matched cohort could further corroborate the results obtained from this study giving a sort of clinical validation of the developed computational approach. Second, a specific screw design has been considered. A different screw design (e.g., cannulated, conical, dual-threaded pedicle screws) could significantly influence the results. For example, a conical screw design provides a larger minor diameter at the thread-shaft junction and intrapedicular portion of the screw. As a consequence, it is reasonable to expect that the conical shape of the screw can reduce the chance for bending failure in this high-stress area compared to the cylindrical shape, leading to a greater strength in flexion (i.e, higher fracture load in flexion). Besides, it has been demonstrated that in healthy vertebrae a dual-thread design significantly improves the pullout strength and allows to achieve an optimal screw stability [28]. As such, a dual-thread design may improve the bone-screw interfacial strength, inducing higher values of fracture load and lower stress concentrations compared to a single thread design. Accordingly, a parametric study based on optimized screw design could impact on future clinical-based engineering studies. Third, the single vertebra analyzed belongs to a non-osteoporotic female patient. As such, the findings of this study may not apply to osteoporotic patients. For such patients, it will be necessary to perform a specific study to account for augmentation with cement, that is often associated with the screw fixation surgery.

Moreover, the ρ_{app}-HU relation (i.e., the calibration equation) has been determined based on the highest HU in the CT scan in a given cortical zone, which is a good-enough approximation for long bones such as femur due to the large amount of cortical bone, especially in the diaphysis. In the vertebra, the cortical layer is very thin and this approach could provide unfaithful parameter estimation. Keaveny et al. [29] developed a patient-specific calibration

approach based on HU values of the external air that is visible on the patient's CT scan and either the patient's blood or adipose tissue. This method may improve model accuracy for vertebrae. Forthcoming studies will be focused on integrating a patient-specific calibration approach for evaluating its influence on the biomechanical response of the spine.

From the constitutive modeling point of view, vertebral bone has been considered as an isotropic and linearly elastic material. This approximation works well at the organ level. However, in the view to account for remodeling processes that characterize bone at different scales, multiscale homogenized constitutive descriptions that include multi-phase material components shall be considered [30]. As such, the present study can be considered a introductory work towards a more in depth constitutive analysis for vertebral bone.

Finally, future work will be focused on developing a model that includes vertebrae and intervertebral disc (i.e., a functional spinal unit, FSU) allowing for a more realistic clinical scenario in terms of boundary conditions and load transfer mechanisms. In this scenario, a single imaging modality (i.e., CT scan) could be unable to provide the necessary information for accurate modeling of both bone and soft tissue structures. FE modeling of the vertebrae and intervertebral disc could require incorporation of data from multiple imaging techniques (i.e. CT, magnetic resonance imaging (MRI) and MR diffusion tensor imaging (DTI)) leading to a more sophisticated geometry definition and constitutive description. The intervertebral disc is characterized by a fibrillar structure such as most of the biological tissues in the human body [31,32], and accounting for the fibers distribution in FE models seems to be fundamental to understand the etiology of degenerative processes and diseases. In this context, DTI may allow us to reconstruct the fiber orientation of the intervertebral disc and thus the anisotropy of such tissue to be incorporated in the FE model [33, 34]. In addition, using a deblurring approach of images, that allows accurate estimates of cortical thickness and intensity [35–37], could improve the cortical layer detection and thus Young's modulus assignment.

Another aspect that should be investigated is related to the pre-stress that the screw insertion procedure generates in the vertebra. This pre-stress may be responsible for a significant alteration of the stress distribution and vertebral fracture mechanisms. To the authors' opinion, the role of pre-stress should be investigated in association with different screw designs. In fact, screws designs may reduce peak localized stress concentrations derived from the insertion phase, making the pre-stress field more uniform at the bone-screw interface and avoiding the generation of localized peak stresses that could have a significant impact on vertebral fracture mechanics. Besides, to the authors' opinion the screw insertion depth influences the pre-stress field. In particular, a shorter insertion can induce localized peak stresses concentrations compared to a deeper insertion that may generate a more distributed stress field at the bone-screw interface.

Appendix A

To derive the density-based E values for the cortical shell of the vertebra, a customized equation (Eq. 5) has been adopted and derived as follows. Five values of ρ_{app} and the corresponding E values have been defined. These pairs have been chosen through a preliminary analysis aiming to obtain for the cortical shell a heterogeneous E distribution with values of Young's modulus in line with the literature (i.e., ranging from 12 to 14 GPa). Then, these pairs have been fitted through a fitting procedure. Among the several fitting relations, a power relationship, that can be expressed in a general form as

$$y = a \times x^b + c \tag{14}$$

has been chosen due to its ability to fit well data with a coefficient of determination R^2 equal to 0.91. In Table 5, the ρ_{app}-E values used to derive the Equation 5 have been reported. The fitting procedure furnished the following coefficients for the power relation expressed by Equation 14: $a = -892.5$, $b = -2.491$ and $c = 14360$.

Table 5 The pairs ρ_{app}-E that have been used to derive the density-elasticity relationship for the cortical bone.

ρ_{app} [g/cm^3]	0.4	0.5	0.6	1	1.8
E [MPa]	8000	9000	10000	13000	15000

Appendix B

In Tables 6 and 7 the p-values of the Shapiro-Wilk test and Levene's test have been reported for the two tested variables, i.e. $\sigma_{\max}$ and σ_{VM}.

Table 6 Shapiro-Wilk and Levene's tests results for screws insertion angles comparison. The variable tested is $\sigma_{\max}$.

Statistical test	Cortical bone	Trabecular bone	Screws
Shapiro-Wilk test	p=0.007	p=0.72	p<0.0001
Levene's test	p=0.5	p=0.06	p=0.7

Table 7 Shapiro-Wilk and Levene's tests results for screws insertion angles comparison. The variable tested is σ_{VM}.

Statistical test	Cortical bone	Trabecular bone	Screws
Shapiro-Wilk test	p=0.0002	p=0.09	p<0.0001
Levene's test	p=0.4	p=0.7	p=0.5

Conflict of interest

The authors declare that they have no conflict of interest.

Acknowledgements Authors acknowledge the support of the Italian National Group for Mathematical Physics (GNFM-INdAM).

References

1. Rutherford E., Tarplett L., Davies E., Harley J., King L., Lumbar spine fusion and stabilization: Hardware, techniques, and imaging appearances, Radiographics, 27, 1737-1749 (2007), doi:10.4329/wjr.v4.i5.193.
2. Chen C.S., Chen W.J., Cheng C.K., Jao S.H.E., Chueh S.C., Wang C.C., Failure analysis of broken pedicle screws on spinal instrumentation, Medical Engineering & Physics, 27, 487-496 (2005), doi:10.1016/j.medengphy.2004.12.007.
3. Sterba W., Kim D.G., Fyhrie D.P., Yeni Y.N., Vaidya R., Biomechanical Analysis of Differing Pedicle Screw Insertion Angles. Clinical biomechanics, 22, 385-91 (2007), doi:10.1016/j.clinbiomech.2006.11.007.
4. Jutte P.C., Castelein R.M., Complications of pedicle screws in lumbar and lumbosacral fusions in 105 consecutive primary operations, European Spine Journal, 11, 594-598 (2003), doi:10.1007/s00586-002-0469-8.
5. Galbusera F., Volkheimer D., Reitmaier S., Berger-Roscher N., Kienle A., Wilke, H.J., Pedicle screw loosening: a clinically relevant complication?, European Spine Journal, 24, 1005-1016 (2015), doi:10.1007/s00586-015-3768-6.
6. Newcomb A.G.U.S., Baek S., Kelly B.P., Crawford N.R., Effect of screw position on load transfer in lumbar pedicle screws: A non-idealized finite element analysis, Computer Methods in Biomechanics and Biomedical Engineering, 20, 1-11 (2017), doi:10.1080/10255842.2016.1209187.
7. Ohba T., Ebata S., Oba H., Koyama K., Haro H., Risk factors for clinically relevant loosening of percutaneous pedicle screws, Spine Surgery and Related Research, 3, 79-85 (2019), doi:10.22603/ssrr.2018-0018.
8. Inceoglu S., Montgomery W.H., St. Clair S., Mclain R., Pedicle screw insertion angle and pullout strength: comparison of 2 proposed strategies, Journal of Neurosurgery. Spine, 14, 670-676 (2011), doi:10.3171/2010.11.SPINE09886.
9. Crawford N.R., Yuksel K.Z., Dogan S., Villasana-Ramos O., Soto-Barraza J.C., Baek S., Porter R.W., Marciano F.F., Theodore N., Trajectory analysis and pullout strength of self-centering lumbar pedicle screws, Journal of Neurosurgery. Spine, 10, 486-491 (2009), doi:10.3171/2009.1.SPINE08274.
10. Jones A.C., Wilcox R.K., Finite element analysis of the spine: Towards a framework of verification, validation and sensitivity analysis, Medical Engineering & Physics, 30, 1287-1304 (2008), doi:10.1016/j.medengphy.2008.09.006.
11. Crawford R.P., Cann C.E., Keaveny T.M., Finite element models predict in vitro vertebral body compressive strength better than quantitative computed tomography, Bone, 33, 744-750 (2003), doi:10.1016/S8756-3282(03)00210-2.

12. Matsukawa K., Yato Y., Imabayashi H., Hosogane N., Asazuma T., Nemoto K., Biomechanical evaluation of the fixation strength of lumbar pedicle screws using cortical bone trajectory: a finite element study, Journal of Neurosurgery: Spine, 23, 471-478 (2015), doi:10.3171/2015.1.SPINE141103.
13. Hussain M., Natarajan R.N., Fayyazi A.H., Braaksma B.R., Andersson G.B.J., An H.S., Screw angulation affects bone-screw stresses and bone graft load sharing in anterior cervical corpectomy fusion with a rigid screw-plate construct: a finite element model study, The Spine Journal, 9, 1016-1023 (2009), doi:10.1016/j.spinee.2009.08.461.
14. Erdem I., Truumees E., Van der Meulen M.C.H., Simulation of the behaviour of the L1 vertebra for different material properties and loading conditions, Computer Methods in Biomechanics and Biomedical Engineering, 16, 736-746 (2013), doi:10.1080/10255842.2011.636741.
15. Fields A.J., Lee G.L., Keaveny T.M., Mechanisms of initial endplate failure in the human vertebral body, Journal of Biomechanics, 43, 3126-3131 (2010), doi:10.1016/j.jbiomech.2010.08.002.
16. Imai K., Analysis of vertebral bone strength, fracture Pattern, and fracture location: A validation study using a computed tomography-based nonlinear finite element analysis, Aging and Disease, 6, 180-187 (2015), doi:10.14336/AD.2014.0621.
17. Falcinelli C., Di Martino A., Gizzi A., Vairo G., Denaro V., Fracture risk assessment in metastatic femurs: a patient-specific CT-based finite-element approach, Meccanica, 55, 861-881 (2020), doi:10.1007/s11012-019-01097-x.
18. Taddei F., Pancanti A., Viceconti M., An improved method for the automatic mapping of computed tomography numbers onto finite element models, Medical Engineering & Physics , 26, 61-69 (2004), doi:10.1016/S1350-4533(03)00138-3.
19. Keyak J.H., Lee I.Y., Skinner H.B., Correlations between orthogonal mechanical properties and density of trabecular bone: use of different densitometric measures, Journal of Biomedical Materials Research, 28, 1329-1336 (1994), doi:10.1002/jbm.820281111.
20. Morgan E.F., Bayraktar H.H., Keaveny T.M., Trabecular bone modulus–density relationships depend on anatomic site, Journal of Biomechanics, 36, 897-904 (2003), doi:10.1016/S0021-9290(03)00071-X.
21. Keller T.S., Predicting the compressive mechanical behavior of bone, Journal of Biomechanics, 27, 1159-1168 (1994), doi:10.1016/0021-9290(94)90056-6.
22. Chen S.I., Lin R.M., Chang C.H., Biomechanical investigation of pedicle screw–vertebrae complex: a finite element approach using bonded and contact interface conditions, Medical Engineering & Physics , 25, 275-282 (2003), doi:10.1016/S1350-4533(02)00219-9.
23. Garfin S., Eismont F.J., Bell G.R., Bono C., Fischgrund M.J., Rothman-Simeone and Herkowitz's The Spine, 2 Vol Set, 2208. Elsevier, (2017)
24. Xu M., Yang J., Lieberman I.H., Haddas R., Finite element method-based study of pedicle screw–bone connection in pullout test and physiological spinal loads, Medical Engineering & Physics, 67, 11-21 (2019), doi:10.1016/j.medengphy.2019.03.004.
25. Zysset P.K., Curnier A., A 3D damage model for trabecular bone based on fabric tensors, Journal of Biomechanics, 29, 1549-1558 (1996), doi:10.1016/0021-9290(96)00087-5.
26. Garcia D., Zysset P.K., Charlebois M., Curnier A., A three-dimensional elastic plastic damage constitutive law for bone tissue, Biomechanics and Modeling in Mechanobiology, 8, 149-165 (2009), doi:10.1007/s10237-008-0125-2.
27. Viceconti M., Olsen S., Burton K., Extracting clinically relevant data from finite element simulations, Clinical Biomechanics, 20, 451-454 (2005), doi:10.1016/j.clinbiomech.2005.01.010.
28. Liu M.Y., Tsai T.T., Lai P.L., Hsieh M.K., Chen L.H., Tai C.L., Biomechanical comparison of pedicle screw fixation strength in synthetic bones: Effects of screw shape, core/thread profile and cement augmentation, Plos ONE, 15, e0229328 (2020), doi:doi.org/10.1371/journal.pone.0229328.
29. Lee D.C., Hoffmann P.F., Kopperdahl D.L., Keaveny T.M., Phantomless calibration of CT scans for measurement of BMD and bone strength — Inter-operator reanalysis precision, Bone, 103, 325-333 (2017), doi:10.1016/j.bone.2017.07.029.
30. Soleimani M., Muthyala N., Marino M., Wriggers P., A novel stress-induced anisotropic growth model driven by nutrient diffusion: Theory, FEM implementation and applications

in bio-mechanical problems, Journal of the Mechanics and Physics of Solids, 144, 104097 (2020), doi:10.1016/j.jmps.2020.104097.
31. Vasta M., Gizzi A., Pandolfi A., On three- and two-dimensional fiber distributed models of biological tissues, Probabilistic Engineering Mechanics, 37, 170-179 (2014), doi:10.1016/j.probengmech.2014.05.003.
32. Vasta M., Gizzi A., Pandolfi A., A spectral decomposition approach for the mechanical statistical characterization of distributed fiber-reinforced tissues, International Journal of Non-Linear Mechanics, 106, 258-265 (2018), doi:10.1016/j.ijnonlinmec.2018.06.010.
33. Falcinelli C., Li Z., Lam W.W., Stanisz G.J., Agur A.M., Whyne C.M., Diffusion-Tensor Imaging Versus Digitization in Reconstructing the Masseter Architecture. Journal of Biomechanical Engineering, 140, 111010-6 (2018), doi:10.1115/1.4041541.
34. Stadelmann M.A., Maquer G., Voumard B., Grant A., Hackney D.B., Vermathen P., Alkalay R.N., Zysset P.K., Integrating MRI-based geometry, composition and fiber architecture in a finite element model of the human intervertebral disc, Journal of the Mechanical Behavior of Biomedical Materials, 85, 37-42 (2018), doi:10.1016/j.jmbbm.2018.05.005.
35. Pakdel A., Robert N., Fialkov J., Maloul A., Whyne C., Generalized method for computation of true thickness and x-ray intensity information in highly blurred sub-millimeter bone features in clinical CT images, Physics in Medicine & Biology, 57, 8099-8116 (2012), doi:10.1088/0031-9155/57/23/8099.
36. Pakdel A., Fialkov J., Whyne C.M., High resolution bone material property assignment yields robust subject specific finite element models of complex thin bone structures, Journal of Biomechanics, 49, 1454-1460 (2016), doi:10.1016/j.jbiomech.2016.03.015.
37. Schileo E., Pitocchi J., Falcinelli C., Taddei F., Cortical bone mapping improves finite element strain prediction accuracy at the proximal femur, Bone, 136, 115348 (2020), doi:10.1016/j.bone.2020.115348.